On the Growth Kinetics of Lamellar and Blocky Austenite during Intercritical Annealing of Hot-Rolled Medium Manganese Steel: Thermodynamic and Diffusion-Controlled Transformation Simulations

R. Surki Aliabad, S. Sadeghpour, P. Karjalainen, J. Kömi, and V. Javaheri

** Materials and Mechanical Engineering, Centre for Advanced Steels Research, University of Oulu Finland (Tel: +358415741507; e-mail: roohallah.surkialiabad@oulu.fi).*

Abstract: Metastable austenite significantly impacts the mechanical properties of Advanced High-Strength Steels (AHSS), especially Medium Mn Steel (MMnS), where its formation rate during intercritical annealing depends strongly on the initial microstructure. This study employs thermodynamic and diffusion-controlled simulations to investigate the formation of two distinct morphologies of retained austenite– lamellar and blocky known also as globular– commonly observed in an intercritically annealed hot-rolled MMnS. Utilizing Thermo-Calc software, coupled with its DIffusion-Controlled TRAnsformation module (DICTRA), phase equilibria are computed, and one-dimensional diffusion equations are solved. Characterization of the microstructure of a medium manganese steel (MMnS) with a nominal composition of Fe–0.4C–6Mn–2Al–1Si–0.05Nb (in wt. %), hot rolled and intercritically annealed for 1 hour at 680°C, was performed using Energy Dispersive Spectroscopy coupled with Transmission Electron Microscopy (EDS-TEM) and Transmission Kikuchi Diffraction (TKD). These techniques were used for experimental validation and verification of the simulations.

Simulations explore the competition between cementite and austenite growth. Specifically, the growth of austenite starting on various interphase boundaries was examined using spherical and planar geometries. This approach resulted in the formation of blocky and lamellar austenite morphologies, respectively. The findings indicate that austenite first nucleates at the BCC/BCC interface and transforms 40% of the BCC phase within 1 second at 680°C. Cementite then starts to form, limiting further austenite transformation. Finally, cementite particles continue to grow to a size of about 100 nm. These simulation results align well with experimental findings.

Keywords: Thermo-Calc, DICTRA, lamellar and blocky austenite, intercritical annealing, Medium Mn Steel.

1. INTRODUCTION

Over the last decade, the demand for strong yet formable steels using cost-efficient designing approaches, contributing to a more sustainable steel advancement, has driven the development of third-generation AHSS (Guo et al., 2022). Among them, MMnS containing 4-12wt% Mn (Han, 2023; Hu et al., 2024; Sun et al., 2023a), is considered the most promising candidate for future steel owing to its unique combination of strength and ductility (Han, 2023). Since its introduction by Miller (Miller, 1972), various alloy design concepts for MMnS have been developed (Han, 2023; Hu et al., 2024; Sun et al., 2023a).

After hot rolling, MMnS exhibits mainly lath martensitic microstructure along with small amounts of retained austenite depending on the Mn content (Han, 2023). Lath martensite represents the predominant morphology in practical high-strength steels. This structure comprises a hierarchical arrangement: martensite packets, blocks, and laths, (Luo et al., 2020; X. Zhang, Miyamoto, Toji, et al., 2018).

When the initial as-rolled martensitic structure undergoes Intercritical Annealing Treatment (IAT), the martensite shows minimal recrystallization throughout the applied thermal cycle. Instead, phase transformations predominantly involve formation of cementite or reversion of austenite (Han, 2023). Martensitic, prior austenitic and BCC/FCC boundaries may endure during intercritical annealing, resulting in several possible nucleation sites for new austenite to form. Additionally, in the tempered martensite microstructure, carbides, particularly cementite, can serve as austenite nucleation sites (Sun et al., 2023b). Austenitic nucleation at these boundaries might result from the co-segregation of C and

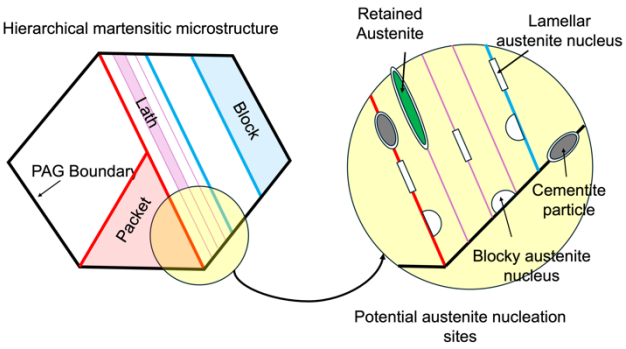

Fig. 1. Illustration of the martensitic hierarchical microstructure and the corresponding preferential austenite nucleation sites.

Mn, which makes them thermodynamically preferred for nucleation (Luo et al., 2011). These nucleation sites can generally be categorized into two groups, as shown in Fig. 1 and described below:

Depending on the location of the nucleus and its orientation with the adjacent martensitic matrix interfaces, two distinct morphologies of austenite may emerge: lamellar and blocky. Lamellar-type austenite typically nucleates at martensite packet, block, or lath boundaries, whereas blocky-type austenite forms at prior austenite grain boundaries, as well as martensite packet and block boundaries (Zhang et al., 2018a). Lamellar austenite grains often display the same orientation as prior austenite grains, which originally form at high temperatures during hot rolling and later coalesce with each other, leading to the reconstitution of the prior austenite grain structure (Han, 2023; Zhang et al., 2018a, 2018b).

Recent multiple-stages MMnS processing routes employ the potential of Mn-rich cementite particles to enhance mechanical properties by providing additional nucleation sites for austenite (Sadeghpour et al., 2021). This tailored austenite differs from conventional formed one, with higher Mn-enrichment and finer size (Ye et al., 2024). Cementite plays complex roles in austenitic nucleation, competing with austenite formation and potentially acting as nucleation sites (Guo et al., 2022). However, not all cementite particles facilitate nucleation; preferential nucleation occurs at intergranular rather than intragranular cementite (Lai et al., 2016). However, Enomoto and Hayashi (Enomoto and Hayashi, 2020) observed a higher fraction of austenite nucleated on cementite existing at prior austenite boundaries and martensite packet boundaries compared to inter-lath boundaries. Additionally, Zhang et al. (Zhang et al., 2021a) suggested that the nucleation potency of cementite particles may depend on their size, with coarser particles expected to have higher potency.

During the IAT, the reverted austenite phase becomes enriched through the partitioning of Mn and C from the surrounding martensite. This gradual enrichment leads to a reduction in the alloy content of nearby martensite, ultimately resulting in its transformation into ferrite. Consequently, after quenching, a significant portion of austenite remains untransformed at ambient temperature (Bhattacharya et al., 2024). Extensive studies have been conducted on various heat treatment parameters such as IA temperature and time (Bansal et al., 2018), as well as tailoring the characteristics of retained austenite (e.g., stability, volume fraction and morphology, etc.) by different IATs (Zhang et al., 2024).

To better understand aspects relevant to intercritical annealing, thermodynamic and kinetic simulations for austenite growth during IAT in the Fe–C–Mn and Fe–C–Mn–Si systems have commonly been conducted. In most of the simulations, a diffusion couple of austenite and martensite was used (Huyan et al., 2018). In this context, the majority of simulations can be summarized into three systems.

FCC/BCC System

Assuming local equilibrium, moving-boundary simulations between austenite and ferrite can provide a simplified representation of austenite growth kinetics. In this system, the diffusional mechanisms of the two phases govern distinct stages of austenite growth. Initially, austenite transformation undergoes rapid increase driven by C diffusion in both ferrite and austenite under negligible partitioning local equilibrium (NPLE) interfacial conditions, with minimal Mn partitioning. Subsequently, a stage dominated by Mn diffusion in ferrite ensues, transitioning from NPLE to partitioning local equilibrium (PLE) interfacial conditions (Sun et al., 2023b). Finally, a slow equilibration of Mn in austenite, controlled by long-range Mn diffusion within austenite, completes the process (Wu et al., 2020).

BCC/FCC/Cementite System

Considering cementite during austenite formation alters the interfacial thermodynamics for austenite growth significantly compared to considering only ferrite and austenite. According to Sun et al. (Sun et al., 2023b), at relatively low intercritical temperatures, when cementite is present in the initial microstructure, austenite growth is primarily controlled by Mn diffusion. Conversely, at higher temperatures, C diffusion governs austenite growth. However, if the initial cementite is enriched with more than 30% Mn, austenite growth remains consistently controlled by Mn throughout the entire intercritical range.

FCC/BCC/Cementite System

Within this system, austenite nucleates apart from the majority of cementite, with the ferrite matrix serving as a pathway for carbon diffusion. Enomoto and Hayashi (Enomoto and Hayashi, 2018) simulated the growth of austenite during continuous heating in plain low-carbon martensite and reported that due to slow carbon diffusivity in austenite, the cementite free of austenite tends to dissolve faster than the cementite on which austenite was nucleated except when the particle size of cementite and/or the number of austenite nuclei is small.

Despite extensive studies on austenite growth and the chemistry of austenite formation on various interfaces in MMnS (e.g., (Dai et al., 2018; Huyan et al., 2018; Mehrabi et al., 2024; Sun et al., 2023b; Zhang et al., 2018b, 2018a), there remains a lack of comprehensive understanding the instance when cementite, austenite and BCC phases are all present during IAT. Hence, we investigated this coexisting scenario in a hot-rolled sample subjected to IAT at 680°C for 1 hour, where two austenite morphologies with cementite particles were observed by microscopic means, by simulating the phase changes by the DICTRA calculations. Further, this study aims to simulate solute partitioning within these microstructures to elucidate the initial source of cementite particles and compare the growth rate of cementite as well as those of lamellar and blocky austenite.

2. MATERIALS AND METHODS

The steel material with the nominal composition of 0.40C, 1Si, 6 Mn, 2Al and 0.05 Nb (wt.%) which employed in this study was produced by OCAS (Onderzoeks Centrum voor de Aanwending van Staal) using a vacuum induction furnace. Following casting, the material underwent austenization at 1200°C for 2 hours, followed by hot rolling to 90 percent

reduction in thickness. The resulting sheet, with a finish rolling temperature of 900°C, was cooled down in ambient air. Subsequently, the sheet underwent intercritical annealing at 680°C for 1 hour.

After standard metallographic sample preparation, the microstructural features of the sample were analyzed using a an TKD mappings using a JEOL JSM-7900F Field Emission Scanning Electron Microscope (FESEM) under an accelerating voltage of 30 kV, a working distance of 15 mm, and a step size of 6 nm. For more comprehensive characterization, elemental analysis of the specimens was carried out using Energy Dispersive x-ray Spectroscopy (EDS) integrated into a 200-kV Energy Filtered Scanning Transmission Electron Microscope (JEOL JEM-2200FS EFTEM/STEM). All of TKD and EDS observations were conducted on a thin lamella sample (8×10 µm) prepared using a Focused Ion Beam-Field Emission Scanning Electron Microscope (FIB-FESEM).

In this study, the DICTRA module of Thermo-Calc 2024a was utilized to model the kinetics of austenite growth, encompassing both lamellar and blocky morphologies with various nucleation sites outlined in Fig. 1. For the simulations, thermodynamic (TCFE7) and mobility (MOBFE2) databases for one-dimensional analyses were used. Establishing the simulations necessitated specifications regarding morphology, compositions, and phase sizes. The diffusion of C, Mn, Si, and Al was factored into the simulation framework. The dimensions of the simulation system were determined based on observed length scales within TKD micrographs obtained from the intercritical annealed sample. The chemical composition of each microconstituent was estimated using EDS method excluding for C.

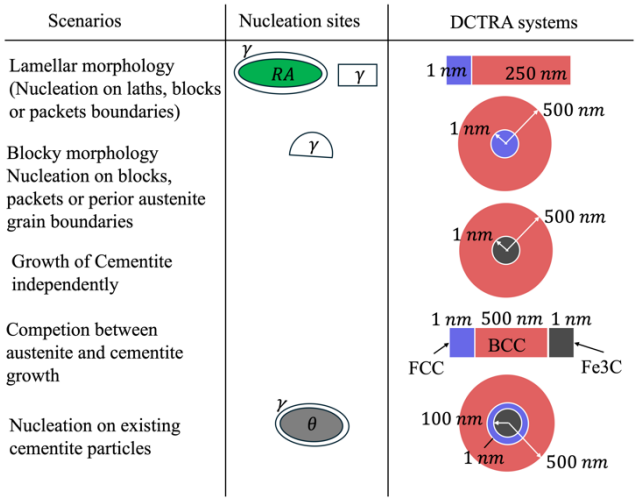

Fig. 2. Schematic illustration of DICTRA simulation configurations based on potential austenite nucleation sites (symbols are described in Fig. 1).

For simulating lamellar and blocky type austenite, planar and cylindrical geometries were respectively adopted. As martensite is not treated as a distinct phase in DICTRA, it is represented similarly to other studies in the literature (Mehrabi et al., 2024), employing a BCC phase with high C and Mn levels. Different simulation configurations based on possible nucleation sites were considered for the DICTRA, as shown in Fig. 2.

3. RESULTS AND DISCUSSION

To model the potential DICTRA systems shown in Fig. 2, the microstructure of the studied steel after the soaking at 680°C for 1 hour were analyzed. The selected timeframe was determined based on our simulations, which suggested that beyond this point, negligible changes in the chemical composition of the solute atoms, particularly Mn, could happen. EBSD-TKD method were employed to obtain the phase map of the microstructure, aiming to discern the distribution and shape of phases and cementite particles. The outcomes of the TKD analysis are depicted in Fig. 2. In this figure, three regions of interest representing the entire microstructure were identified. Fig. 2(b) clearly shows a lamellar microstructure, with the austenite lamellae approximately 200 nm in width and the BCC phase lamella with widths of 300 nm. The half-width dimensions as a preliminary estimation of the system size were used. Additionally in Fig. 3(c), a typical illustration of blocky austenite morphology is depicted. This structure is encompassed by adjacent BCC grains, forming an outer circle with a radius of 500 nm and an inner circle with a radius of 300 nm. Essentially, around 60% of the BCC phase transforms into austenite within this system.

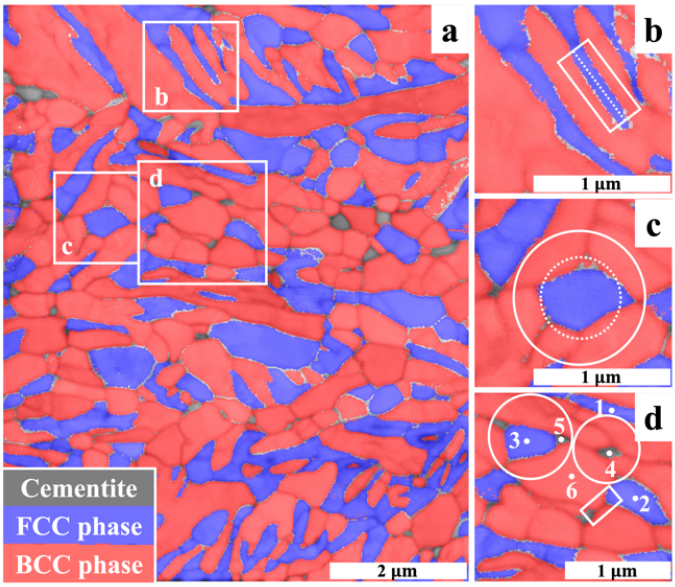

Fig. 3. a) TKD phase map with band contrast image highlighting three regions of interest (b, c, and d) used to define five different DICTRA systems introduced in Fig. 2. In (d), the numbers indicate the regions which their chemical composition determined by EDS (Table 1).

In Fig. 3(d), two distinct configurations of cementite particles depending on their position with the BCC and austenite phases are highlighted. In one arrangement, austenite and cementite are juxtaposed, possibly indicating the nucleation of austenite on cementite surfaces. Additionally, isolated cementite particles are observable within the BCC matrix, some reaching diameters of several hundred nanometers. Close observation of the particles adjacent to austenite grains reveals that most of

them have diameters less than 100 nm after the IAT, whereas those farther from austenite regions generally have diameters exceeding 200 nm.

The efficacy of cementite particles in promoting austenite nucleation has been shown highly dependent on their size, with maximum nucleation potency observed in particles with diameters between 100 and 200 nm (Zhang et al., 2021b). Particles larger or smaller than this range do not significantly contribute to the nucleation process. This suggests that, at the beginning of IAT, we might have had particles within the nucleation size range, but they partially dissolved during IAT. Conversely, the particles now larger than 200 nm and isolated in the BCC matrix likely did not engage in the austenite nucleation process.

Figure 4(a) illustrates the time-dependent variation in the fraction of transformed austenite under different scenarios by according to the DICTRA simulation. Curves b (red) and c (blue) depict results for lamellar and blocky austenite, respectively, which nucleated and grew at the BCC/BCC interface. Additionally, curves d (shown in solid and dashed black lines) indicates the growth kinetics of cementite particles that formed at the BCC/BCC interface but grew independently of austenite.

In curves b and c, the initial rapid increase in the fraction transformed is attributed to the growth of austenite under NPLE conditions. However, this NPLE stage is usually not observed experimentally under typical intercritical annealing conditions (Sun et al., 2023b). During this stage, growth is governed by carbon diffusion in ferrite. Over time, the carbon distribution in the ferrite matrix becomes progressively more homogeneous (Wei et al., 2013). Consequently, the growth of austenite becomes increasingly controlled by the carbon diffusion within the austenite until the diffusion of substitutional atoms, particularly Mn, begins to occur under the PLE conditions. The later stage comprises three separate steps (Luo et al., 2011). The corresponding interfacial boundary position at this stage can be considered as the size of the intercritical austenite observable experimentally.

Numerical simulations on the diffusion couples FCC/BCC (Fig. 4(a), curves b and c) indicate that the phase fraction of the formed austenite (for both the lamellar and blocky morphologies) after 1 hour of annealing at 680°C should increase up to 0.7. However, this fraction is generally much higher than what is calculated based on Fig. 3(a), showing about 0.38 area fraction.

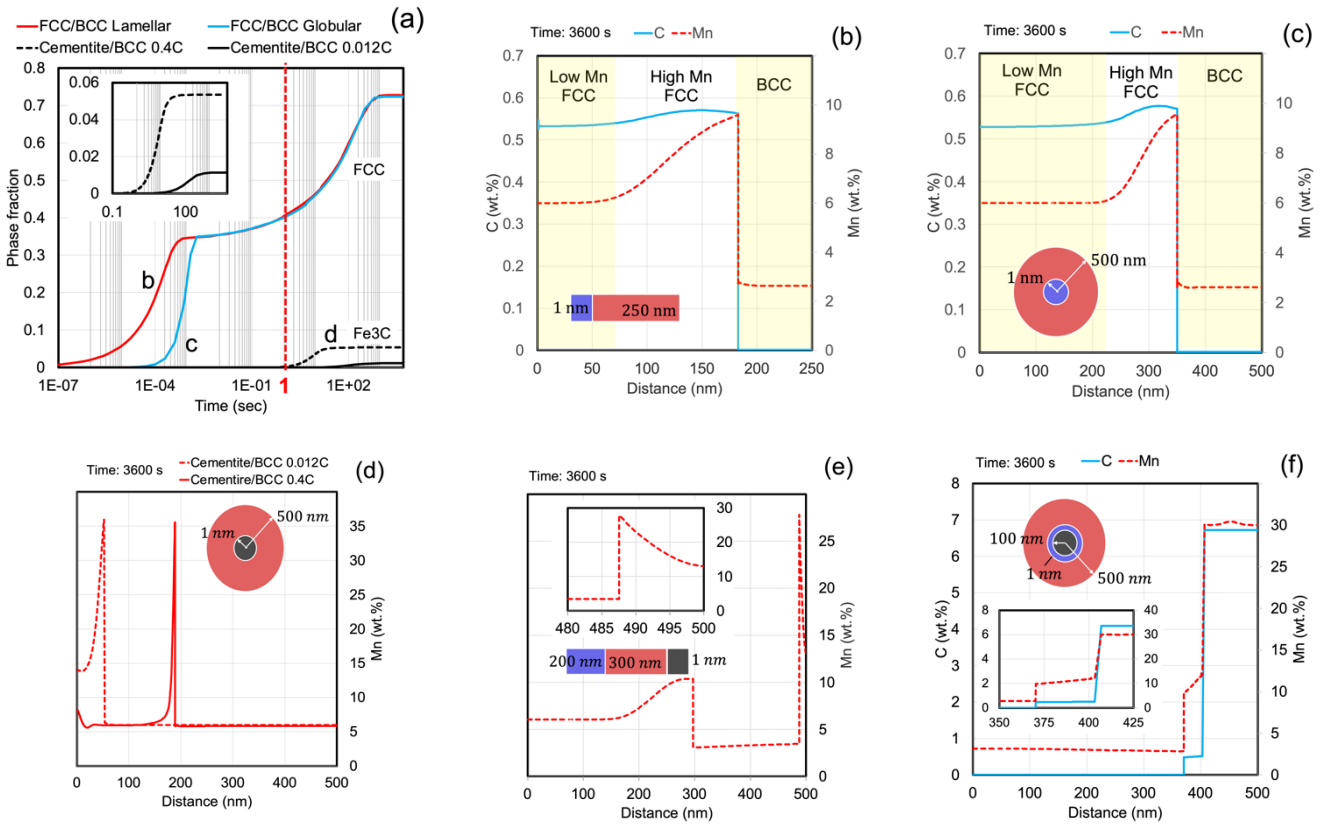

Fig. 4. a) Comparison of simulated volume fractions of austenite and cementite using DICTRA. Concentration profiles of C and Mn are shown for different growth scenarios: (b) lamellar austenite growth from the BCC/BCC interface, (c) blocky austenite growth from the BCC/BCC interface, (d) comparison of cementite growth and Mn distribution in the BCC phase with two different carbon contents 0.4 and 0.012 wt.%, (e) simultaneous growth of pre-existing austenite and cementite into the BCC matrix, and (f) growth of austenite at the Cementite/BCC interface based on chemical composition measured by EDS (Table 1).

DOI: 10.3384/ecp212.028

There could be two explanations for this deviation: the interfacial dissipation energy due to finite interface mobility at the austenite/martensite interface (Huyan et al., 2018), and consumption of C and Mn due to formation of cementite after one second of annealing. the latter will be discussed in the following sections.

Comparing the growth rates of lamellar and blocky austenite during the NPLE stage, it is observed that lamellar austenite grows more quickly than blocky austenite does, even when simulations are conducted for both morphologies with the same system size (250 nm). This difference in the growth rate can be attributed to the larger surface area provided by the lamellar structure, which facilitates more efficient carbon diffusion and thereby accelerates the austenite growth. However, both morphologies exhibit the same PLE stage due to the sluggish diffusion of Mn, which cannot be compensated for even with a higher diffusion area. This slow Mn diffusion controls the overall transformation kinetics at this stage.

According to the simulation results, the concentration of Mn should be highly non-uniform in the austenite, particularly in the instance of the blocky morphology. Fig. 4(b) and (c) also indicate that the Mn flux into the austenite remains confined to the region near the boundary, with a maximum of 9.6 wt.%, even after a long holding time. However, the experimental results show a deviation in both Mn concentration and distribution profile. A comparison between chemical composition of different microconstituents, which are marked by numbers in Fig. 3(d), is shown in Table 1.

Table 1. Chemical composition of the regions defined in Fig. 3d

Point	Region of interest	Mn	Al	Si
1	Lamellar austenite	12.13	1.21	0.56
2	Blocky austenite	11.16	1.15	0.69
3	austenite formed on cementite	11.12	1.11	0.71
4	Cementie in BCC matrix	29.74	0.27	0.19
5	Cementite in the vicinity of FCC	29.24	0.19	0.19
6	BCC phase	3.91	1.79	0.98

Figure 4(d) shows two different scenarios of cementite growth for 1 hour annealing. As shown in this figure, two initial carbon levels for the BCC matrix were considered for the simulation. First, we supposed cementite forms in a region far from austenite, where all alloying elements only engage in its growth. It can be seen that there is a very marginal concentration of Mn at the cementite/BCC interface. Consequently, a thickness of 10 to 20 nm and a total cementite diameter of about 400 nm should be formed in the microstructure. However, in the experimental results, we could not find any cementite with such a large size and high Mn gradient.

On the other hand, Fig. 4(a) shows that from a BCC matrix with 0.4% C, cementite would start to grow after about 1 second of annealing, during which most of the carbon in the BCC matrix carbon is consumed by austenite formation. At this point, the BCC carbon concentration lowers to about 0.012 wt.%, but other elements still retain their nominal composition far from the interface in both sides. For the second scenario, we used 0.012% C for the simulation of the growth of new cementite simulation growth, assuming that at first 40 percent of the BCC matrix transformed into austenite and then cementite separately forms in the remaining matrix. In this scenario, the austenite, cementite, and BCC phases seem to have their chemical compositions closer to the experimental results (Table 1), and also their sizes correspond to those depicted in Fig. 3(a) and (d).

At this point (after 1 second of annealing), another scenario could be considered: a competition between the formation of cementite and the simultaneous growth of pre-existing austenite. Fig. 4(e) illustrates the results for this co-existing scenario and the corresponding system size. In this scenario, cementite and austenite are both forming and growing at the same time. The simulation reveals that after 1 hour of holding at 680°C, cementite can only grow 10 nanometers.

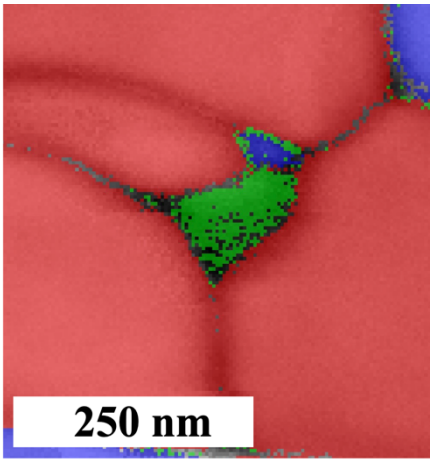

Fig. 5. EBSD-TKD phase map with band contrast image showing austenite, less than 50 nm in size, formed on a cementite particle with a 200 nm diameter after 1 hour of soaking at 680°C (austenite: blue, cementite: green and BCC in red color).

This limited growth could be due to the simultaneous consumption of carbon and other alloying elements by both cementite and austenite. As a result, the growth rate of austenite is also reduced compared to a system where only FCC/BCC transformations occur without the presence of cementite. Moreover, the simulation indicates that the Mn content in cementite, under these conditions, would be less than 20 wt.% in average. This is significantly lower than the Mn content measured by EDS, suggesting that the actual distribution of Mn is more complex than the simulation predicts. This discrepancy further implies that the interaction between cementite and austenite formation is more intricate, affecting the distribution and concentration of alloying elements. In summary, the co-existence scenario shown in Fig. 4e suggests that while cementite formation limits its own growth and the growth of austenite, it does not fully account for the experimentally observed austenite sizes and Mn concentrations. The competition between cementite and austenite growth, along with the resultant elemental distributions, highlights the complexity of phase transformations in these materials.

Additionally, Fig. 4f illustrates a scenario based on experimental results where the cementite particle size and the chemical composition of BCC and cementite were measured directly using TKD and EDS methods. In this scenario, we assumed that austenite would form at the Cementite/BCC interface, as observed in Fig. 5. However, the simulation results shown in Fig. 4f suggest that this scenario does not account for the formation of large blocky austenite grains. The simulation indicates that within holding for 1 hour, the austenite can only grow to a size of 30 nm. In contrast, the measured austenite diameter in Fig. 3d is approximately 700 nm, demonstrating a significant discrepancy. This discrepancy suggests that the big austenite grain does not primarily form at the Cementite/BCC interface. Instead, austenite likely forms initially within the FCC/BCC system separately. Over time, these austenite grains may coalesce with austenite that nucleates at the Cementite/BCC interface, leading to the larger blocky austenite grains observed experimentally.

5. CONCLUSIONS

In this study, various scenarios were simulated to better understand the microstructure observed and analyzed using EBSD-TKD and EDS methods after annealing of a hot-rolled 0.40C-6 Mn-1Si-2Al-0.05 Nb steel at 680°C for 1 hour. The aim was to approximate the system size and chemical composition of each microconstituent, including lamellar austenite with a thickness of 100 to 200 nm, blocky austenite with a radius of approximately 500 nm, and cementite particles, either adjacent to austenite or dispersed in the BCC matrix.

The DICTRA software was used to simulate five potential systems to determine which of them could be responsible for the existing microstructure. The following systems were simulated:

- FCC/BCC system
- Cementite/BCC with 0.4% C in the matrix and Cementite/BCC with 0.012% C in the matrix (both assuming cementite growth without the influence of austenite)
- Two co-existing austenite and cementite systems (adjacent and separate from each other, considering the competition between austenite and cementite).

Based on comparison of the results from the simulations and experimental observations, it seems highly likely that austenite nucleates first at the BCC/BCC interfaces and grows, leading to the transformation of 40% of the BCC phase to austenite within 1 s at 680°C. Then, the cementite formation occurs, which ceases the further growth of austenite as a competitor. Following this, only cementite continues to grow under these circumstances. Notably, after 1 hour of annealing at 680°C, the experimental results show that 38% austenite exists in the microstructure, and the size of cementite particles is about 100–200 nm, which align well with the above hypothesis.

ACKNOWLEDGMENTS

The authors would like to thank Jane ja Aatos Erkon säätiö (JAES) and Tiina ja Antti Herlinin säätiö (TAHS) for their financial supports on Advanced Steels for Green Planet project.

REFERENCES

Bansal, G.K., Madhukar, D.A., Chandan, A.K., Ashok, K., Mandal, G.K., Srivastava, V.C., (2018). On the intercritical annealing parameters and ensuing mechanical properties of low-carbon medium-Mn steel. Materials Science and Engineering: A 733, 246–256. doi: 10.1016/j.msea.2018.07.055

Bhattacharya, A., Biswal, S., Barik, R.K., Mahato, B., Ghosh, M., Mitra, R., Chakrabarti, D., (2024). Comparative interplay of C and Mn on austenite stabilization and low temperature impact toughness of low C medium Mn steels. Mater Charact 208. doi: 10.1016/j.matchar.2024.113658

Dai, Z., Ding, R., Yang, Z., Zhang, C., Chen, H., (2018). Elucidating the effect of Mn partitioning on interface migration and carbon partitioning during Quenching and Partitioning of the Fe-C-Mn-Si steels: Modeling and experiments. Acta Mater 144, 666–678. doi: 10.1016/j.actamat.2017.11.025

Enomoto, M., Hayashi, K., (2020). Simulation of Austenite Formation During Continuous Heating from Low Carbon Martensite with Poly-dispersed Cementite. Metall Mater Trans A Phys Metall Mater Sci 51, 618–630. doi: 10.1007/s11661-019-05569-3

Enomoto, M., Hayashi, K., (2018). Modeling the growth of austenite in association with cementite during continuous heating in low-carbon martensite. J Mater Sci 53, 6911–6921. doi: 10.1007/s10853-018-2020-2

Guo, Q., Hu, B., Luo, H., (2022). Mechanism and Application of Reverse Austenitic Transformation in Medium Mn Steels: A Systematic Review. Steel Res Int 93, 2200257. doi: 10.1002/srin.202200257

Han, J., (2023). A Critical Review on Medium-Mn Steels: Mechanical Properties Governed by Microstructural Morphology. Steel Res Int 94, 2200238. doi: 10.1002/srin.202200238

Hu, B., Sui, H., Wen, Q., Wang, Z., Gramlich, A., and Luo, H. (2024). Review on the plastic instability of medium-Mn steels for identifying the formation mechanisms of Lüders and Portevin–Le Chatelier bands. International Journal of Minerals, Metallurgy and Materials. doi: 10.1007/s12613-023-2751-1

Huyan, F., Yan, J.Y., Höglund, L., Ågren, J., and Borgenstam, A., (2018). Simulation of the Growth of Austenite from As-Quenched Martensite in Medium Mn Steels. Metall Mater Trans A Phys Metall Mater Sci 49, 1053–1060. doi: 10.1007/s11661-018-4497-3

Lai, Q., Gouné, M., Perlade, A., Pardoen, T., Jacques, P., Bouaziz, O., and Bréchet, Y., (2016). Mechanism of Austenite Formation from Spheroidized Microstructure in an Intermediate Fe-0.1C-3.5Mn Steel. Metall Mater Trans A Phys Metall Mater Sci 47, 3375–3386. doi: 10.1007/s11661-016-3547-y

Luo, H., Shi, J., Wang, C., Cao, W., Sun, X., and Dong, H. (2011). Experimental and numerical analysis on formation of stable austenite during the intercritical annealing of 5Mn steel. Acta Mater 59, 4002–4014. doi: 10.1016/j.actamat.2011.03.025

Mehrabi, A., Zurob, H.S., and McDermid, J.R., (2024). Process Maps for Predicting Austenite Fraction (vol.%) in Medium-Mn Third-Generation Advanced High-Strength Steels. Materials 17. doi: 10.3390/ma17050993

Miller, R.L. (1972). Ultrafine-grained microstructures and mechanical properties of alloy steels. Metallurgical Transactions 3, 905–912. doi: 10.1007/BF02647665

Sadeghpour, S., Somani, M.C., Kömi, J., and Karjalainen, L.P. (2021). A new combinatorial processing route to achieve an ultrafine-grained, multiphase microstructure in a medium Mn steel. Journal of Materials Research and Technology 15, 3426–3446. doi: 10.1016/j.jmrt.2021.09.152

Sun, B., Kwiatkowski da Silva, A., Wu, Y., Ma, Y., Chen, H., Scott, C., Ponge, D., and Raabe, D. (2023). Physical metallurgy of medium-Mn advanced high-strength steels. International Materials Reviews 68, 786–824. doi: 10.1080/09506608.2022.2153220

Wei, R., Enomoto, M., Hadian, R., Zurob, H.S., and Purdy, G.R. (2013). Growth of austenite from as-quenched martensite during intercritical annealing in an Fe-0.1C-3Mn-1.5Si alloy. Acta Mater 61, 697–707. doi: 10.1016/j.actamat.2012.10.019

Wu, Y.X., Wang, L.Y., Sun, W.W., Styles, M.J., Studer, A.J., Bréchet, Y., Arlazarov, A., and Hutchinson, C.R. (2020). Austenite formation kinetics from multicomponent cementite-ferrite aggregates. Acta Mater 196, 470–487. doi:10.1016/j.actamat.2020.07.001

Ye, Q., Dong, H., Guo, Q., Yu, Y., Qiao, L., and Yan, Y. (2024). Tailoring the austenite characteristics via dual nanoparticles to synergistically optimize the strength-ductility in cold rolled medium Mn steel. J Mater Sci Technol 169, 158–171. doi: 10.1016/j.jmst.2023.07.002

Zhang, X., Miyamoto, G., Kaneshita, T., Yoshida, Y., Toji, Y., and Furuhara, T., (2018). Growth mode of austenite during reversion from martensite in Fe-2Mn-1.5Si-0.3C alloy: A transition in kinetics and morphology. Acta Mater 154, 1–13. doi: 10.1016/j.actamat.2018.05.035

Zhang, X., Miyamoto, G., Toji, Y., Nambu, S., Koseki, T., and Furuhara, T., (2018). Orientation of austenite reverted from martensite in Fe-2Mn-1.5Si-0.3C alloy. Acta Mater 144, 601–612. doi: 10.1016/j.actamat.2017.11.003

Zhang, X., Miyamoto, G., Toji, Y., Zhang, Y., and Furuhara, T., (2021). Role of cementite and retained austenite on austenite reversion from martensite and bainite in Fe-2Mn-1.5Si-0.3C alloy. Acta Mater 209. doi: 10.1016/j.actamat.2021.116772

Zhang, Y., Ye, Q., and Yan, Y., (2024). Processing, microstructure, mechanical properties, and hydrogen embrittlement of medium-Mn steels: A review. J Mater Sci Technol. doi: 10.1016/j.jmst.2024.03.014